



# Two-step synthesis of Ag-decorated MoO<sub>3</sub> nanotubes, and the effect of hydrogen doping

M. Sajadi<sup>a,b</sup>, M. Ranjbar<sup>b,\*</sup>, R. Rasuli<sup>a</sup>

<sup>a</sup> Department of Physics, Faculty of Science, University of Zanjan, Zanjan, Iran

<sup>b</sup> Department of Physics, Isfahan University of Technology, Isfahan 8415683111, Iran

## ARTICLE INFO

### Keywords:

MoO<sub>3</sub>  
Nanosheets  
AgNO<sub>3</sub>  
MoO<sub>3</sub> nanotubes  
Localized surface plasmon resonance  
Hydrogen

## ABSTRACT

Nowadays, plasmonic nanomaterials have become more attractive owing to their enhanced surface sensitivity towards species adsorption. Here we report on Ag-decorated MoO<sub>3</sub> nanotubes (Ag-MNTs) were obtained via a straightforward two-step process, involving anodizing synthesis of blue MoO<sub>x</sub> nanosheets in water, followed by adding an AgNO<sub>3</sub> complex. It was observed that, depending on the Ag:Mo molar ratio, the solution bleached to light green or brown colors. Based on TEM, XRD, UV–Vis, Raman spectroscopy, and XPS, we found that this is due to a process in which MoO<sub>x</sub> nanosheets transform into MoO<sub>3</sub> nanotubes (MNTs), and formation of Ag NPs decorated on those nanotubes. The Ag–MoO<sub>3</sub> colloidal solutions achieved were sensitive to hydrogen injection as the color return to a light green/blue color. Our data show that the Mo oxide stoichiometry is reversible in a hydrogenation/dehydrogenation cycle. But the structure of MNTs collapses due to the interaction with hydrogen. However, the real-time hydrogen doping was studied by UV–Vis spectrometry on sealed hydrogenated solutions. This process led to a spectral shift in Ag plasmonic peak, and change in the absorption strength with a correlation to Ag:Mo molar ratio, and MoO<sub>x</sub> LSPR absorption, which was assumed to be proportional to the hydrogen doping level.

## 1. Introduction

Tubular nanostructures have been extensively studied after carbon nanotube discovery by Iijima, owing to their high surface to volume ratio, and outstanding applications in nanodevices [1]. Moreover, decoration of CNTs by noble metal nanoparticles such as Pd, Au, and Ag, has gained their properties capability, for instance, in the catalytic and sensing applications [2–6]. On the one hand, synthesis of nanotubular systems other than CNTs, particularly metal oxides, has been reported in recent years, but they require certain control over the synthesis conditions. Similar to CNTs, decoration of metal oxide nanotubes with a variety of nanoparticles has also been used to enhance their surface functionality via facilitating charge transfer with target materials such as adsorbed gases [7–9].

Molybdenum oxide, as an exceptional material, has been known to have different nanoscale structures, including sheet, and nanotube morphologies. Since the first report on Mo oxide single-walled nanotubes in 2008 [10], they have been explored by different groups owing to their potential applications in environmental science, catalysis, displays, and gas sensors. Mo oxide nanotubes are of particular interest as they can be produced from an initial nanosheet phase thanks to their

interlayer Van der Waals forces [11]. Two-dimensional molybdenum oxide extensively investigated as an *n*-type semiconductor material [12–15]. For example, Q. Huang et al. have reported the synthesis of white MoO<sub>3</sub> NTs from as-synthesized blue MoO<sub>x</sub> nanosheets by oleamine molecules, and oxidants [11]. J. V. Silveira et al. have prepared MNTs by a hydrothermal method, and investigated their thermal stability [16]. In 2010, M. Suemitsu et al. published a paper on rectangular MoO<sub>2</sub> nanotubes by combustion-flame methods [17]. Transformation of nanowires [18,19], and vacuum heating of Mo foils [20] was also reported for Mo oxide nanotube formation. However, the decoration of Mo oxide nanotubes with metal nanoparticles has not been reported vastly. Particularly, combining the plasmonic properties of a noble metal with chemical reactivity of Mo oxide nanotubes is interesting for developing the plasmonic-based sensing material library [21,22]. Among the noble metal nanoparticles, Ag NPs exhibit a visible LSPR absorption band suitable for colorimetric sensing [23–25], which originates from collective electron oscillation at a resonant frequency [26–29]. The wavelength at which LSPR occurs depends on surrounding properties, particle size/shape, and degree of particle agglomeration [30–33].

MoO<sub>3</sub> has been known for its oxidation ability to reduce gases such

\* Corresponding author.

E-mail address: [ranjbar@cc.iut.ac.ir](mailto:ranjbar@cc.iut.ac.ir) (M. Ranjbar).

<https://doi.org/10.1016/j.apsusc.2020.146675>

Received 28 March 2020; Received in revised form 5 May 2020; Accepted 10 May 2020

Available online 01 June 2020

0169-4332/ © 2020 Elsevier B.V. All rights reserved.

as hydrogen as an explosive energy source of the future [34–39]. In the case of hydrogen, lattice oxygen atoms involve in reaction with hydrogen leading to change in the physical, chemical, and morphological properties of  $\text{MoO}_3$ . In combination with plasmonic nanoparticles, any of these variations can lead to detectable spectral shift, and optical absorption strength of the plasmonic material [40–43]. Thanks to their optical base, plasmonic phenomena can provide a safer detection method for hydrogen sensing demands comparing with resistive based sensors. Also, the plasmonic effect is very sensitive to the surface adsorption of molecules. Until now, many researchers have reported the development of noble metal plasmonic gas sensors to detect hydrogen gas [44–46].

Our previous works demonstrated how the colloidal solution of the blue  $\text{MoO}_x$  nanosheets could be obtained by a facile, and scalable method of anodizing the Mo electrodes in an acidic electrolyte [47,48]. It was shown that this product can reduce  $\text{PdCl}_2$  and  $\text{HAuCl}_4$  directly to metallic nanoparticles for plasmonic hydrogen detection, solar heat shielding, and photochromic. In this paper, we discovered that when  $\text{AgNO}_3$  complex is used,  $\text{MoO}_x$  nanosheets convert to MNTs that are decorated with Ag NPs. As will be discussed further, these nanotubes can be destructed after hydrogen doping resulting in change in the plasmonic properties of adhered Ag counterpart. TEM, XRD, XPS, and UV–Vis were used for characterization.

## 2. Materials and methods

$\text{MoO}_x$  nanosheets were produced by a facile electrochemical anodizing method which was reported in our previous works [47,48]. In this approach, we used a 0.02 M HCl solution in DI water as an electrolyte. Two Mo metallic rods with 2 mm diameter and purity of 99.99% were placed 1 cm separated in the prepared electrolyte. Then a 30 V DC voltage was applied to the electrodes for 10 min (Fig. 1). As a result, the  $\text{MoO}_x$  nanosheets are exfoliated and released in the electrolyte. The concentration of the colloid solution was measured from the weight loss of the anode molybdenum rod. The colloidal  $\text{MoO}_x$  nanosheets solutions were centrifuged at 5000 rpm for 15 min, and the precipitates were dried at 50 °C in air. Finally, the  $\text{MoO}_x$  powder was dissolved in DI water and sonicated for 5 min.

An aqueous solution of  $\text{AgNO}_3$  ( $10^{-3}$  M) was prepared by dissolving 0.67 gr of  $\text{AgNO}_3$  (99.99%, Sigma Aldrich Inc.) in 1000 ml DI water. Different ratios of Ag:Mo molar ratio including 1:50, 1:40, 1:25, 1:20, 1:10, and 1:5 were prepared by adding  $\text{AgNO}_3$  to the  $\text{MoO}_x$  solution. The samples are named as the ratio of silver to molybdenum, for example, as  $\text{S}_{1:5}$ . Then Ag ions reduced by  $\text{MoO}_x$  nanosheets (Fig. 1) and formed Ag NPs. To investigate the effect of the hydrogen gas, we poured 10 ml of each sample into a vessel bottle, and the air of the flask was evacuated with a vacuum pump until the solution starts to bubble. Then 60 ml of 10%  $\text{H}_2/\text{Ar}$  gas was inserted into the vessel. For TEM, XRD,

Raman, and XPS analysis, samples were allowed to exposed to air after hydrogen exposure. Therefore, for these analyses, a hydrogenation/dehydrogenation process was applied to samples.

UV–Vis spectroscopy was performed by the Perkin Elmer spectrophotometer (Lambda 25). XRD patterns were recorded using a Philips XPERT X-ray diffractometer unit with  $\text{Cu K}\alpha$  radiation. TEM imaging was performed with the Philips Holland model CM120. X-ray photoelectron spectroscopy (XPS) was conducted using an ESCA/AES system (Specs model EA10 plus). Raman spectroscopy was performed using an Ocean Optics QE6500 spectrometer, with a 532 nm laser as the excitation source, and a notch filter utilized to prevent signals below  $100\text{ cm}^{-1}$ . The detailed study of hydrogen doping into  $\text{MoO}_x$  structures was made possible by UV–Vis spectroscopy. To do this, we injected hydrogen into the sealed cuvette cells, and then the spectra were acquired.

## 3. Results and discussion

### 3.1. TEM

Fig. 2 shows the TEM images of the initial blue  $\text{MoO}_x$  nanosheets and the obtained  $\text{Ag-MoO}_3$ , before and after the hydrogenation/dehydrogenation process. The initial blue  $\text{MoO}_x$  NPs involve nanosheet structures of  $> 200\text{ nm}$  lateral dimension. In addition, many smaller flake-like particles of about  $40\text{ nm}$  were also observable in different parts of the sample. From part (b), one can observe that addition of  $\text{AgNO}_3$  complex leads to transformation of  $\text{MoO}_x$  nanosheets into tubular structures that, as will be shown by XPS spectra, have  $\text{MoO}_3$  composition. It should be noted that all the reactions were done in water, and room temperature, hence this approach can be considered as a green synthesis method. The MNTs have an outer diameter of about  $30\text{ nm}$  and a thickness of about  $8\text{ nm}$ . As TEM clearly shows, many spherical Ag nanoparticles with an average of  $4\text{ nm}$  were adhered to the MNTs. The Ag crystallite could be identified by both the XRD and XPS analysis. However, TEM images in part (c) show that MNTs were completely destroyed by hydrogen exposure so that tubular structures are no longer observed after hydrogenation/dehydrogenation process. Hydrogen-induced cross-linking of Mo–O bonds would be expected to occur through the MNTs collapse into fine fragments. As a result of nanotube destruction, the degree of Ag NPs agglomeration seems also to somewhat change.

### 3.2. XRD and UV–Vis

X-ray diffraction was used to further confirm the formation of metallic Ag NPs (Fig. 3(a)(I)). For the blue  $\text{MoO}_x$  sample, the diffraction peaks at  $2\theta = 23.05^\circ$ , and  $26.35^\circ$  are associated with the (0 1 1), and (1 1 1) orientations of  $\text{MoO}_x$  monoclinic phase (JCPDS No. 37–1445).

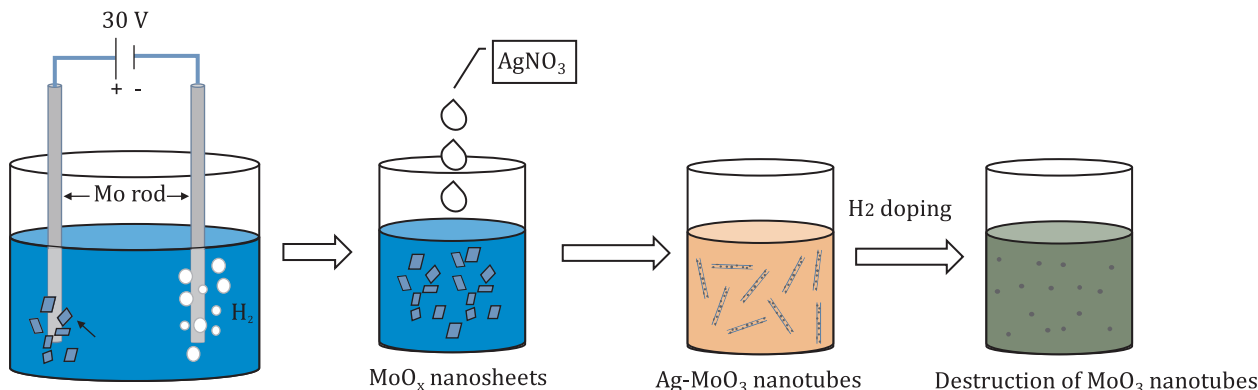


**Fig. 1.** Schematic representation of the synthesis procedure of blue  $\text{MoO}_x$  nanosheets by anodizing method, the addition of  $\text{AgNO}_3$  that results in the formation of Ag-MNTs, and finally, hydrogen doping, and nanotube destruction.

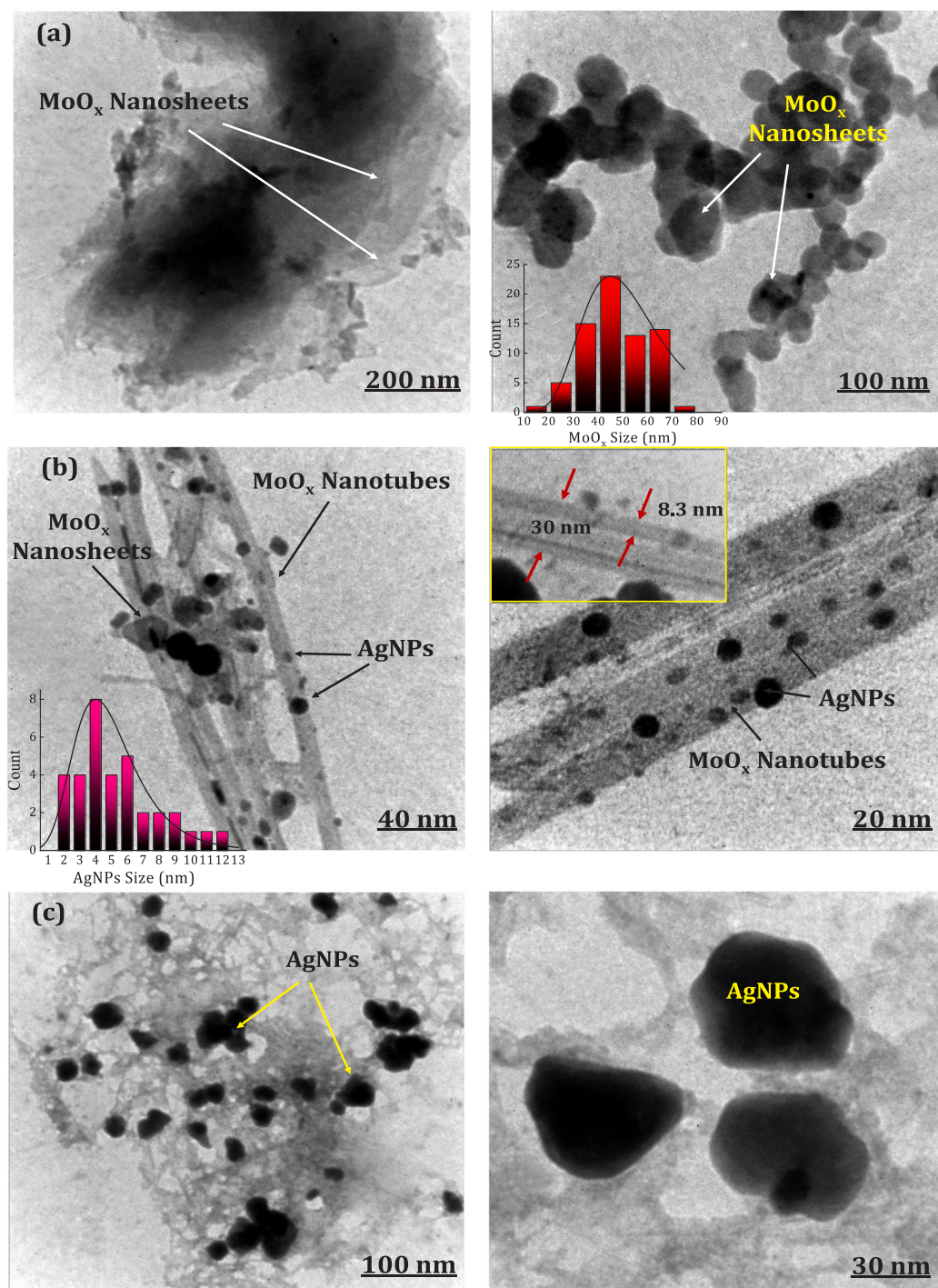


**Fig 2.** TEM images of (a) the initial blue colloids of MoO<sub>x</sub> before, and (b) after adding AgNO<sub>3</sub> complex, sample S<sub>1.5</sub>. As a result, Ag-MNTs are produced. (c) destruction of the nanotubes in part (b) due to hydrogen doping.

XRD pattern of the Ag-MoO<sub>3</sub> sample (sample S<sub>1.5</sub> in part (II)) reveals formation of the metallic silver structure. The diffraction at 37.9°, 44.1°, 64.6, and 77.5° are related to the cubic phase of silver (JCPDS No. 04-0783) (Fig. 3 (a)(II)). After the hydrogenation/dehydrogenation cycle, the crystalline structure of the silver nanoparticles is preserved, as shown in Fig. 3(a)(III), indicating that the H<sub>2</sub>-air exposure cycle does not affect the silver counterpart structure. Therefore, silver nanoparticles exhibit good stability in this process. The Mo oxide diffraction peaks are no longer visible in these two patterns, probably due to a low degree of crystallinity. Therefore, Raman spectra were used to examine more closely the structural changes of molybdenum oxide.

The optical absorption spectra of the blue MoO<sub>x</sub> before and after mixing with the AgNO<sub>3</sub> solution are shown in Fig. 3(b). An LSPR absorption band is observed at about 740 nm before mixing, which is due to oscillation from free electrons of defective MoO<sub>x</sub> structure. After adding 10<sup>-3</sup> M, the AgNO<sub>3</sub> solution (S<sub>1.5</sub> Ag:Mo molar ratio), the blue solution bleaches to green, and, after two hours, to light brown. On the other hand, an LSPR absorption peak appears at 433 nm, which is characteristic of silver nanoparticles. As can be seen, the LSPR band of the MoO<sub>x</sub> disappears at the same time, which is discussed in more detail in the next sections. The effect of hydrogen on the optical changes of colloidal solutions is presented in more detail later in the next parts.



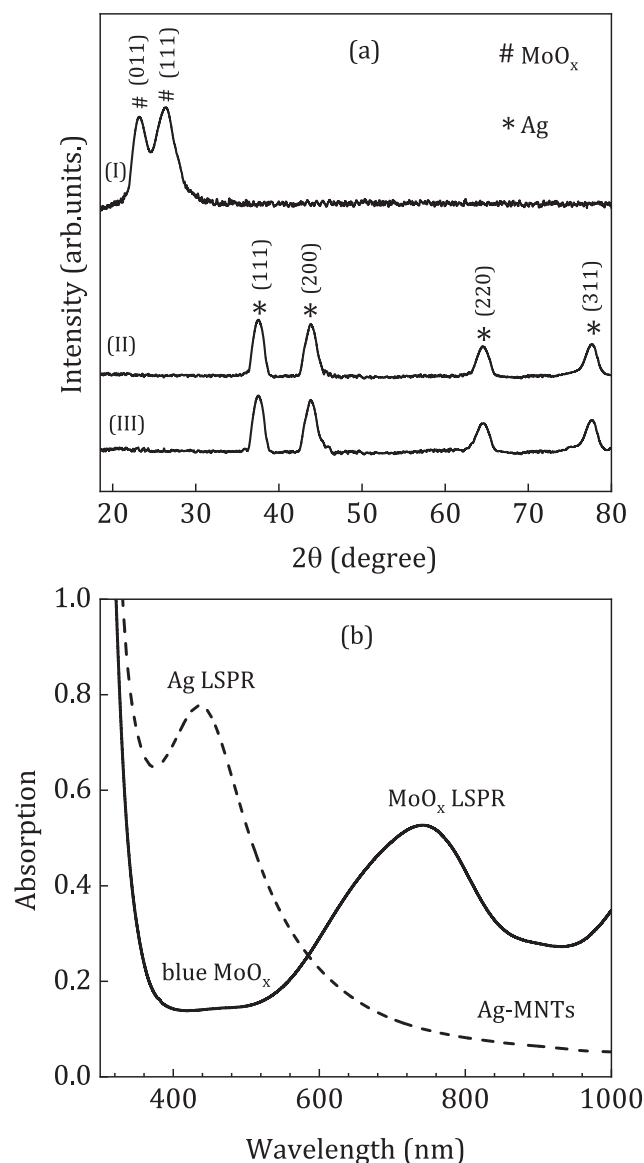


**Fig. 3.** (a) XRD patterns of (I) the initial blue MoO<sub>x</sub> nanosheets, (II) after adding AgNO<sub>3</sub> (Ag-decorated MoO<sub>3</sub> sample S<sub>1.5</sub>), (III) part (II) after 1 cycle H<sub>2</sub>-air exposure. (b) Optical absorption spectra of the initial blue MoO<sub>x</sub> and Ag-MNTs (S<sub>1.5</sub>).

### 3.3. Raman spectroscopy

Since XRD could not detect the structural variations in our Mo oxide part, the initial blue MoO<sub>x</sub> and Ag-decorated nanotubes were further analyzed by Raman spectroscopy (Fig. 4). The peak at 988 cm<sup>-1</sup> represents the terminal oxygen (Mo=O) stretching mode, which is assigned to unshared O atoms. The peaks at 807 cm<sup>-1</sup> is illustrated for the double coordinated oxygen (Mo<sub>2</sub>-O) in asymmetric stretching mode, which are due to the corner-sharing oxygen atoms common to two MoO<sub>6</sub> octahedral. Besides, peaks at 650 cm<sup>-1</sup> is related to the triply coordinated oxygen (Mo<sub>3</sub>-O) asymmetric stretch mode. This mode illustrates the edge-shared oxygen atoms between three adjacent octahedral. The 280, and 376 cm<sup>-1</sup> peaks are also assigned to the bending mode of Mo=O vibration. Raman spectra show that after adding AgNO<sub>3</sub>, the relative intensities of peaks at 988 cm<sup>-1</sup>, 947 cm<sup>-1</sup> (Mo=O), and 898 cm<sup>-1</sup> (O=Mo=O) reduce. Therefore, after mixing with silver nitride, the double bonds have become weaker, which is consistent with the oxidation of the initial defective blue MoO<sub>x</sub> phase [36,49]. It should be noted that we did not find a significant change in

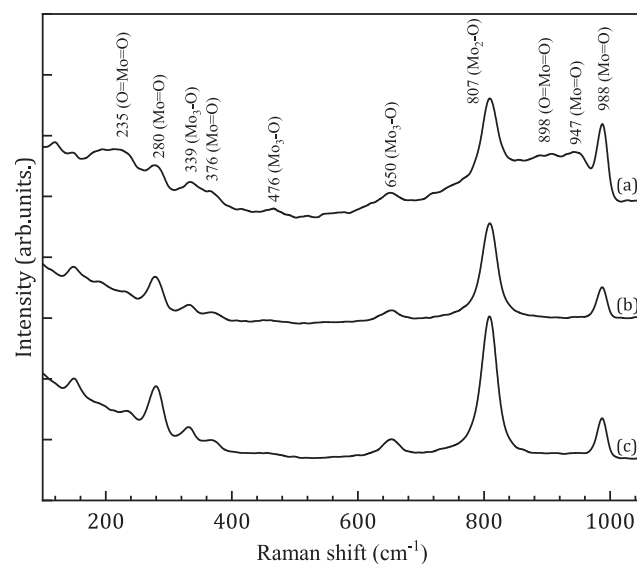


**Fig. 4.** Raman spectra of (a) the initial blue MoO<sub>x</sub> nanosheets, and (b) Ag-MNTs (sample S<sub>1.5</sub>), and (c) part (b) after one cycle H<sub>2</sub>-air exposure.

the Raman spectrum due to the hydrogenation/dehydrogenation process (part (c)). This may be due to the hydrogen removal from the molybdenum oxide structure during air exposure prior to transfer to the Raman system. Such results show a reversibility in the hydrogenation process, which may be suitable for sensing applications.

### 3.4. Xps

XPS was used to investigate the variations of the elements' chemical states (Fig. 5). The binding energies and FWHM values obtained from the high-resolution XPS spectra are also presented in Table.1. Fig. 5(a) shows the survey scan spectra, which consist of Mo3d, O1s, and carbon contaminants peaks at their defined positions. For the Ag-MoO<sub>3</sub> sample, the XPS peaks of Ag also appear which evidence formation of Ag nanostructures. As shown in Fig. 5, for the initial blue MoO<sub>x</sub> dispersion, there are two Mo3d doublets at different binding energies. The peaks at 232.6, and 235.7 eV correspond to 3d<sub>3/2</sub>, and 3d<sub>5/2</sub> core levels of Mo<sup>+6</sup>, and 231.6, and 234.7 eV are related to Mo<sup>+5</sup> states [50,51]. After adding silver counterpart, which led to nanotube formation, the Mo3d XPS spectrum exhibits only two peaks located at 232.7, and 235.8 eV, corresponding to Mo<sup>+6</sup> states in MoO<sub>3</sub> stoichiometric composition. Therefore, transformation of nanosheets into nanotubes is accompanied by the oxidation of Mo<sup>5+</sup> into Mo<sup>6+</sup> indicating nanotubes have MoO<sub>3</sub> phase. From Table.1 XPS binding energies and corresponding FWHM of different elements, the Mo3d becomes narrower as FWHM of 1.5–1.5 to 1.3–1.4, respectively, which is due to the lowering of Mo<sup>5+</sup> percentage [48]. After hydrogenation/dehydrogenation cycle, the Mo3d peak position remains almost unchanged. The slight increase in FWHM to 1.5 and 1.6 eV may be evidence for partial reduction of Mo<sup>+6</sup> to Mo<sup>5+</sup>.

As shown in Fig. 5, the binding energy of Ag3d is located at 368.3 and 374.3 eV, in good agreement with metallic Ag NPs [52]. After the hydrogen/dehydrogenation process, binding energies shift only slightly to 368.9, and 374.5 eV. The binding energy of O1s in pure MoO<sub>x</sub> shows two peaks at 530.7 and 533.5 eV with FWHM of 2.0 and 2.1 eV, respectively. The former peak is corresponding to the lattice oxygen of the Mo-O bond, and the later one reveals the presence of surface hydroxyl groups [53]. For the Ag-MoO<sub>3</sub> sample, the peaks in the O1s spectrum shift to 530.6, and 532.4 eV with FWHM of 1.5, and 2.4 eV. As is shown, the hydroxyl peak is much stronger than that of lattice. However, after adding AgNO<sub>3</sub>, the relative intensity of hydroxyl peak decrease considerably. This result suggests that the initial blue nanosheets may have a partial hydrate phase of Mo oxide [53]. For after hydrogenation/

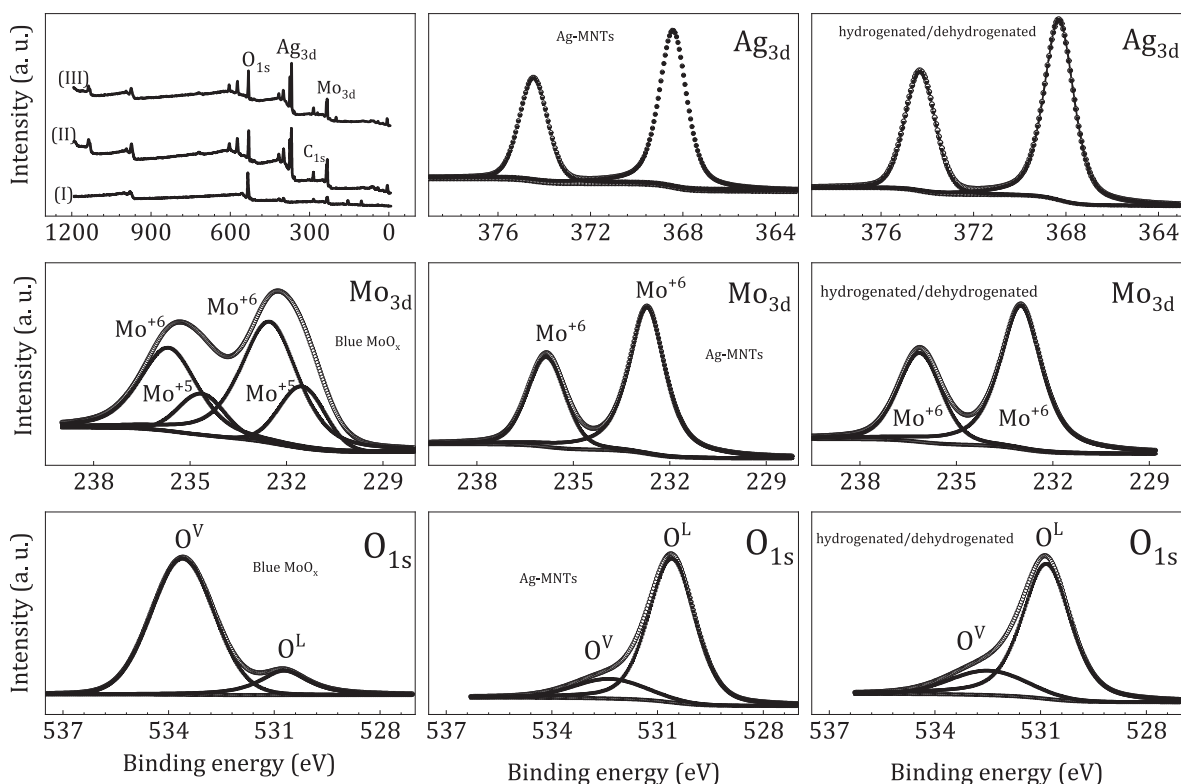


**Fig 5.** XPS spectra of (I) blue MoO<sub>x</sub>, (II) Ag-MNTs (S<sub>1.5</sub>) before, (III) after 1 cycle H<sub>2</sub>-air exposure. Corresponding high-resolution XPS spectra of Ag<sub>3d</sub>, Mo<sub>3d</sub>, and O<sub>1s</sub> are also presented.

**Table 1**

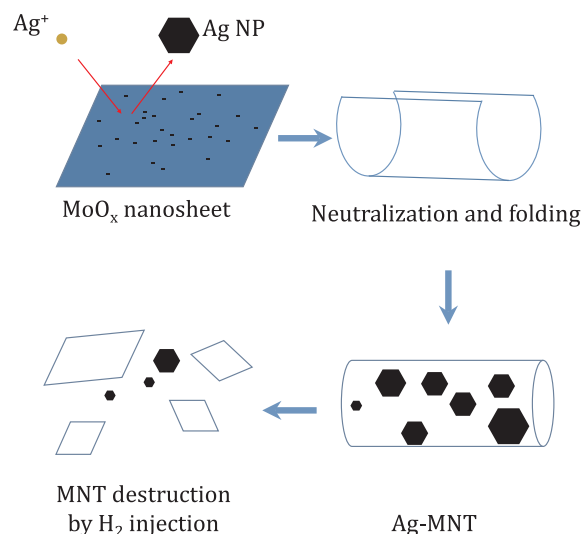
XPS binding energies, and corresponding FWHMs of different elements for the initial blue MoO<sub>x</sub>, and sample S<sub>1.5</sub>.

Sample	Core level	B.E (eV)	FWHM (eV)
Initial blue MoO <sub>x</sub>	Mo <sub>3d</sub>	232.6–235.7	2.5–2.5
		231.6–234.7	2.5–2.5
	O <sub>1s</sub>	530.7–533.5	2.0–2.1
Ag-MNTs (S <sub>1.5</sub> )	Mo <sub>3d</sub>	232.7–235.8	1.3–1.4
	Ag <sub>3d</sub>	368.3–374.3	1.5–1.5
	O <sub>1s</sub>	530.6–532.4	1.5–2.4
S <sub>1.5</sub> after hydrogenation/dehydrogenation	Mo <sub>3d</sub>	233–236.1	1.5–1.6
	Ag <sub>3d</sub>	368.9–374.5	1.4–1.4
	O <sub>1s</sub>	530.83–532.5	1.6–2.6

dehydrogenation, the two O<sub>1s</sub> peaks are located at 530.8 and 532.5 eV with FWHMs of 1.6 and 2.6 eV. Similarly, the Mo-O peak is also dominant in this case. It can be attributed to the injection of hydrogen in the structure of MoO<sub>3</sub> and the formation of hydroxyl groups [48].

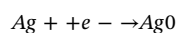
### 3.5. The formation, and destruction of MNTs mechanism

Fig. 6 illustrates schematically a proposed mechanism for formation of Ag decorated Mo oxide nanotubes. Mo oxide has various oxidation states, and in substoichiometric compositions can behave as a conductor. The blue MoO<sub>x</sub> nanosheets obtained by anodizing exfoliation method have a lot of defect sites [54], which prevent them from folding. The positively charged silver cations receive electron as they reach the MoO<sub>x</sub> oxygen vacancy sites. Thus, MoO<sub>x</sub> is oxidized, and Ag ions reduce to metallic Ag NPs. As reported elsewhere, the oxidation of Mo<sup>+5</sup> to Mo<sup>+6</sup> removes the blue color of the initial dispersion [55], and Ag NPs with a yellowish color are obtained. Ag nucleus gradually grow to form nano-sized Ag NPs. Formation of Ag NPs simultaneously with MoO<sub>x</sub> oxidation is responsible for appearing plasmonic absorption of Ag, and weakening of MoO<sub>x</sub> NIR absorption. The



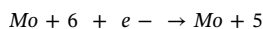
**Fig 6.** Schematic representation of Ag-MNT formation from reaction of AgNO<sub>3</sub> with MoO<sub>x</sub> nanosheets, and destruction by H<sub>2</sub> injection.

following half-reactions describe the possible process [56]:



Additionally, as a result of charge transfer in this oxidation–reduction reaction, the Coulomb repulsion forces across the sheets are eliminated, leading to rising surface tension and generating driving force for the rolling-up of nanosheets [11]. These observations suggest that the oxidation reaction on blue Mo oxide nanosheets not only bleaches them due to Mo<sup>5+</sup> → Mo<sup>6+</sup> conversion but also leads to great changes in morphology, and the structure of Mo oxide NPs.

Fig. 6 schematically represents also the destruction of MNTs into smaller fragments in the hydrogenation process. In general, the mechanism of hydrogen doping induced fragmentation of the MNTs is explained as follows: the AgNPs catalytically dissociate the  $H_2$  molecules into proton-electrons pairs, which intercalates into the  $MoO_3$  lattice, and then OH groups, and  $H_xMoO_3$  phase are formed. As a result, the Mo-O bonds are broken significantly, and the nanotubes destroy into smaller fragments [49]. The process of the reduction of  $Mo^{6+}$  cations to  $Mo^{5+}$  by hydrogen is also expected according to the following reactions:



Therefore, the reduction of  $Mo^{6+}$  into  $Mo^{5+}$  can be directly due to hydrogen doping. It has been known that there is a correlation between the color of colloids containing Mo oxide, and the  $Mo^{5+}/Mo^{6+}$  ratio. In our case, the appearance of green or blue color is a result of hydrogen-induced  $Mo^{6+} \rightarrow Mo^{5+}$  conversion.

Moreover, in the hydrogen-doped  $MoO_3$ , reduction of  $MoO_3$  into  $H_xMoO_3$  occurs usually. However, according to literature, when x exceeds 1 formation of  $Mo^{4+}$  is expected [57]. In addition, at higher concentrations, formation of hydrogen free  $MoO_2$  can occur. Our XPS results could not trace  $Mo^{4+}$  states, therefore  $H_2MoO_3$  phase formation, cannot be directly proved based on the presented data. For a detailed investigations based on  $Mo^{4+}$  states, the hydrogen-reduced samples should be analyzed without being exposed to air to keep any  $H_xMoO_3$  phase during analysis. Also, due to the fact that our Mo oxide nanoparticles are very small and have no XRD diffraction peaks, we cannot prove the formation or non-formation of this phase with ordinary analyzes. However, there are several papers investigating the hydrogen reduction of  $MoO_3$  [58–62]. For example, Takeshi Matsuda et al. have mentioned in a paper [62] that that reduction of  $MoO_3$  at temperature below 623 K proceeded via the formation of  $H_xMoO_3$ , while  $MoO_3$  was directly converted to  $MoO_2$  at 673 K. Any of this conversions are accompanied by an increase in oxygen vacancies, and the level of a free carrier concentration of  $MoO_x$  particles, leading to appearing a NIR (750 nm in our case) LSPR absorption band [48].

It should be noted that in general, hydrogen can change the morphology of molybdenum oxide, which, for example, depends on temperature. Takeshi Matsuda et al. have reported surface area enlargement by hydrogen interaction with  $MoO_3$  [62]. Jie Dang et al have studied the phase transition and morphology evaluation of  $MoO_3$  to  $MoO_2$  by hydrogen from 678 to 829 K, which undergoes an intermediate  $Mo_4O_{11}$  phase [63]. T. Ressler et al [64] have reported  $MoO_3 \rightarrow MoO_2$  transition occurs at above 600 K. These papers show that a temperature of more than 600 K is required to change the phase and change the morphology without the presence of a catalyst. However, according to our results, it seems that in Ag-decorated  $MoO_3$  nanotubes, hydrogen can change the morphology of the molybdenum oxide even at room temperature.

### 3.6. The effect of Ag:Mo molar ratio on the optical properties

Representative photographic images, and UV–Vis absorption spectra of the Ag- $MoO_x$  dispersions with different Ag:Mo molar ratios are shown in Fig. 7(a). When it increases from 0.02 ( $S_{1:25}$ ) to (0.2)  $S_{1:5}$ , the relative intensity of the  $MoO_x$  LSPR peak decreases and finally diminishes. At the same time, the appearance of Ag LSPR peak at about 430 nm occurs, indicating the formation of silver colloids with nanoscale size. According to Beer-Lambert law [65], the peak intensities are assumed to be proportional with Ag, and defective  $MoO_x$  ratio, respectively. The Ag:Mo absorption ratio vs. the Ag:Mo molar ratio plot (part(b)) exhibits a linear behavior, indicating a good correlation between concentrations, and the optical absorption.

The formation of Ag NPs can be better understood in terms of the Ag

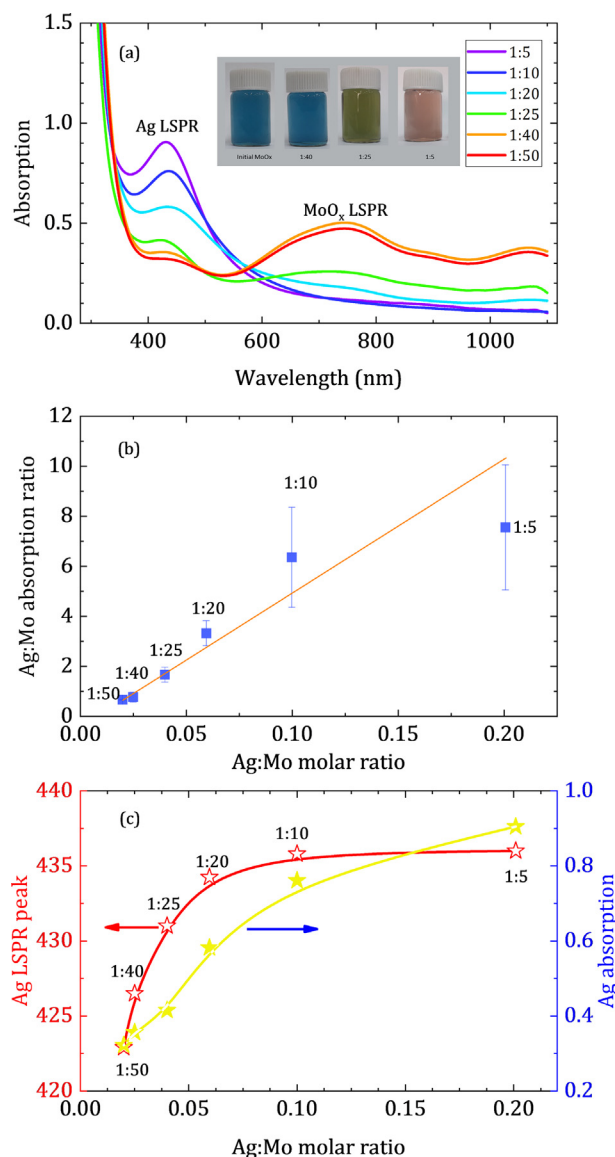
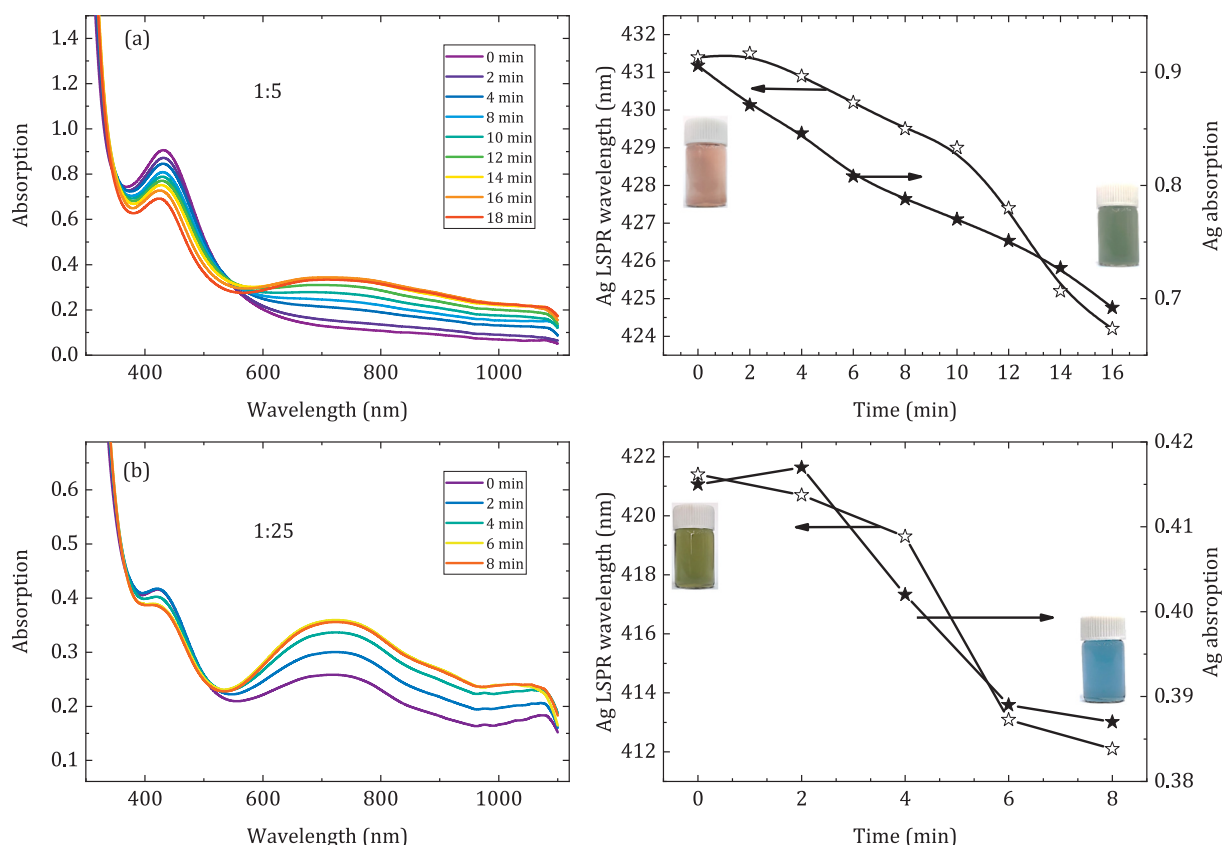


Fig. 7. (a) Optical absorption spectra of Ag- $MoO_x$  dispersions with different Ag:Mo molar ratio. The right panel shows three typical images. (b) Ag:Mo absorption intensity v.s. Ag:Mo molar ratio. (c) Ag LSPR peak wavelength (left vertical axis), and Ag absorption (right axis) as a function of Ag:Mo molar ratio.

LSPR characteristics. Fig. 7(c) shows the wavelength and absorption intensity of the Ag LSPR plotted vs. Ag:Mo molar ratio. The Ag peak redshifts from 422 to 435 nm as the Ag:Mo molar ratio increases from 0.02 to 0.05, and then saturates by a further increase of ratio to 0.2. Almost the same behavior exists for absorption. This behavior suggests that when silver nitride exceeds a certain content; its reduction does not proceed further, and probably requires more Mo content. The images taken from the solution on adding  $AgNO_3$  indicates that the initial blue color turns green or brown as the Ag content increases.

### 3.7. Hydrogen-doping

In the previous part, we attempted to demonstrate that there is a correlation between Ag LSPR characteristics and the defect level in the substoichiometric  $MoO_x$  NPs. On the other hand, hydrogen doping can increase the free carrier concentration in metal oxides [66,67], which can be quantified by the LSPR absorption in the case of plasmonic metal oxides like  $MoO_3$ . One can assume the change in the intensity of  $MoO_x$  LSPR absorption is proportional to the hydrogen intercalation level



**Fig 8.** Optical absorption spectra Ag-MoO<sub>x</sub> solutions for (a) sample S<sub>1:5</sub>, and (b) sample S<sub>1:25</sub>. Right panels indicate the time variation of the Ag LSPR position and intensity for each sample at different times after 10% H<sub>2</sub> injection.

[34], thereby it can be used as a platform to measure the hydrogen concentration in their surroundings. To do this, we injected the same volumes of 10% H<sub>2</sub> gas into the same volumes of solutions containing S<sub>1:5</sub> (high Ag content), and S<sub>1:25</sub> (low Ag content). Because the hydrogen penetration into the structure of metal oxide nanoparticles is gradual, the optical absorption spectra were recorded each 2 min. This way allows us to compare the absorption characteristics of Ag LSPR peaks in terms of different levels of hydrogen doping in the MoO<sub>3</sub> part. For sample S<sub>1:5</sub> shown in Fig. 8(a), the initial brown visual color of the Ag NPs dispersion converts to light green, indicating the formation of Mo<sup>5+</sup> states. In this figure, a blue-shift from 431.5 nm to 424 nm is observable. At the same time, the Ag intensity reduces, and the MoO<sub>x</sub> LSPR band emerges and grows again at about 750 nm. In the case of sample S<sub>1:25</sub>, the initial color is green, which turns blue on hydrogen injection (Fig. 8(b)). Due to increased Mo oxide content, the NIR LSPR peak is stronger in the sample than the previous sample, and the Ag LSPR peak can be found at 421.5 nm. Therefore, similar behavior is observed for sample S<sub>1:25</sub> (part (b)), except in the Ag peak position and relative intensities. In the right panel, the time variation plot of the position and intensity of the Ag peak indicates a decreasing trend. However, the behavior of sample S<sub>1:5</sub> is more linear, and also it has a greater possible data points comparing with the other sample.

To our best knowledge, no report exists on MoO<sub>3</sub> nanotube reaction with hydrogen. However, common MoO<sub>3</sub> powder, without supporting catalyst, react with hydrogen at elevated temperatures [62]. Ag NPs can act as a hydrogen catalyst for MoO<sub>3</sub> to react with hydrogen at room temperature.

In Fig. 9, the Ag LSPR peak absorption strength, and wavelength are plotted as a function of MoO<sub>x</sub> LSPR absorption intensity, which reveals the decreasing behavior for both the LSPR position and absorption. Fig. 9 reveals that the optical characteristics of Ag absorption peak correlate with the MoO<sub>x</sub> LSPR absorption intensity, hence the hydrogen

doping level. However, sample S<sub>1:5</sub> has better linearity behavior. These results suggest that the Mo content should probably be kept as low as possible compared to Ag content to provide a better calibration curve. Taken together, our results show that in the silver molybdenum oxide system, one can obtain information about the concentration of hydrogen injection into the molybdenum oxide structure by tracing the silver absorption peak.

It is very instructive to inject different concentrations of hydrogen gas into the optimum solution and investigate their sensing characteristics. However, in a sensing tool, various parameters such as response, response/recovery times, reversibility, repeatability, and selectivity all need to be investigated, it requires an extensive study that will be published in our future articles.

#### 4. Conclusion

We demonstrated that defective MoO<sub>x</sub> nanosheets could transform into MoO<sub>3</sub> nanotube structures decorated with NPs of a reduction agent cations. When a noble metal such as Ag is decorated, it can be used for an LSPR gas sensing, especially when the nanotubes can be destroyed in the presence of gas. In this study, a good correlation for Ag LSPR intensity, and wavelength was observed in the detection of hydrogen gas. In summary, we attempted to develop a noble-metal decorated metal-oxide nanotubes concept for gas sensing applications.

#### CRediT authorship contribution statement

**M. Sajadi:** Conceptualization, Methodology, Software. **M. Ranjbar:** Data curation, Writing - original draft. **R. Rasuli:** Supervision.



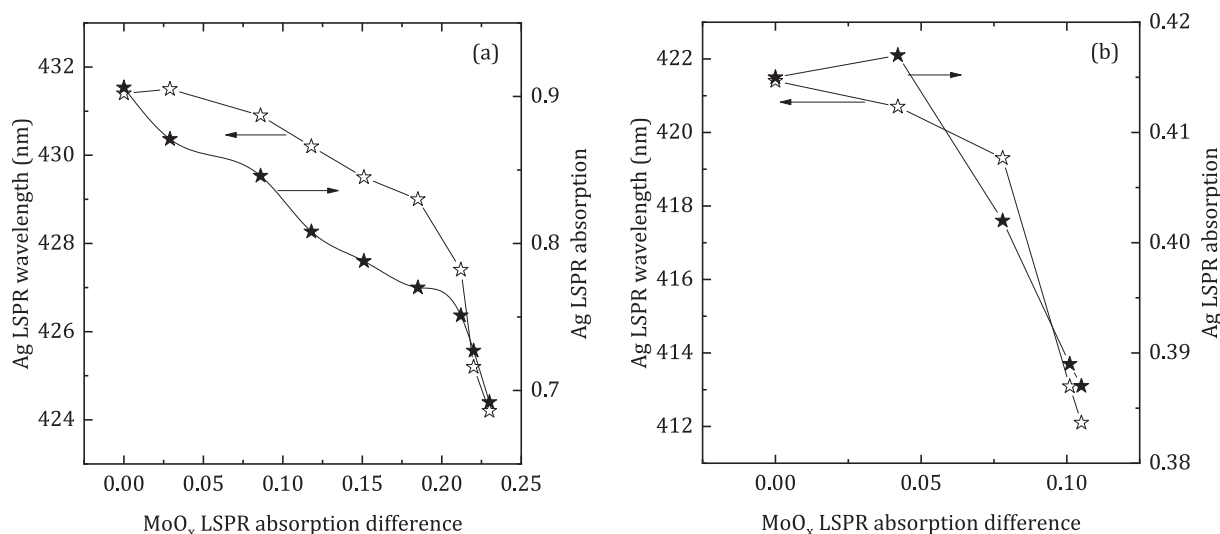


Fig 9. Ag LSPR wavelength and absorption plots vs. absorption change of MoO<sub>x</sub> LSPR peak. (a) sample S<sub>1:5</sub>, and (b) sample S<sub>1:25</sub>.

## Declaration of Competing Interest

The authors declare that they have no known competing financial interests or personal relationships that could have appeared to influence the work reported in this paper.

## References

- [1] S. Iijima, Helical microtubules of graphitic carbon, *Nature* 354 (1991) 56–58, <https://doi.org/10.1038/354056a0>.
- [2] H. Chu, Y. Shen, L. Lin, X. Qin, G. Feng, Z. Lin, J. Wang, H. Liu, Y. Li, Ionic-liquid-assisted preparation of carbon nanotube-supported uniform noble metal nanoparticles and their enhanced catalytic performance, *Adv. Funct. Mater.* 20 (2010) 3747–3752, <https://doi.org/10.1002/adfm.201001240>.
- [3] E.H. Espinosa, R. Ionescu, C. Bittencourt, A. Felten, R. Erni, G. Van Tendeloo, J.J. Pireaux, E. Llobet, Metal-decorated multi-wall carbon nanotubes for low temperature gas sensing, *Thin Solid Films* 515 (2007) 8322–8327, <https://doi.org/10.1016/j.tsf.2007.03.017>.
- [4] V. Georgakilas, D. Gournis, V. Tzitzios, L. Pasquato, D.M. Guldi, M. Prato, Decorating carbon nanotubes with metal or semiconductor nanoparticles, *J. Mater. Chem.* 17 (2007) 2679–2694, <https://doi.org/10.1039/b700857k>.
- [5] M. Scarselli, L. Camilli, P. Castrucci, F. Nanni, S. Del Gobbo, E. Gauron, S. Lefrant, M. De Crescenzi, In situ formation of noble metal nanoparticles on multiwalled carbon nanotubes and its implication in metal-nanotube interactions, *Carbon N. Y.* 50 (2012) 875–884, <https://doi.org/10.1016/j.carbon.2011.09.048>.
- [6] A. Star, V. Joshi, S. Skarupo, D. Thomas, J.C.P. Gabriel, Gas sensor array based on metal-decorated carbon nanotubes, *J. Phys. Chem. B* 110 (2006) 21014–21020, <https://doi.org/10.1021/jp064371z>.
- [7] B.E. Sanabria-Arenas, A. Mazare, J. Yoo, N.T. Nguyen, S. Hejazi, H. Bian, M.V. Diamanti, M.P. Pedferri, P. Schmuki, Intrinsic AuPt-alloy particles decorated on TiO<sub>2</sub> nanotubes provide enhanced photocatalytic degradation, *Electrochim. Acta* 292 (2018) 865–870, <https://doi.org/10.1016/j.electacta.2018.09.206>.
- [8] S.N. Basahel, K. Lee, R. Hahn, P. Schmuki, S.M. Bawaked, S.A. Al-Thabaiti, Self-decoration of Pt metal particles on TiO<sub>2</sub> nanotubes used for highly efficient photocatalytic H<sub>2</sub> production, *Chem. Commun.* 50 (2014) 6123–6125, <https://doi.org/10.1039/c4cc01287a>.
- [9] S. Zhang, B. Peng, S. Yang, H. Wang, H. Yu, Y. Fang, F. Peng, Non-noble metal copper nanoparticles-decorated TiO<sub>2</sub> nanotube arrays with plasmon-enhanced photocatalytic hydrogen evolution under visible light, *Int. J. Hydrogen Energy* 40 (2015) 303–310, <https://doi.org/10.1016/j.ijhydene.2014.10.122>.
- [10] S. Hu, X. Wang, Single-walled MoO<sub>3</sub> nanotubes, *J. Am. Chem. Soc.* 130 (2008) 8126–8127, <https://doi.org/10.1021/ja801448c>.
- [11] Q. Huang, S. Hu, J. Zhuang, X. Wang, MoO<sub>3</sub>-x-based hybrids with tunable localized surface plasmon resonances: Chemical oxidation driving transformation from ultrathin nanosheets to nanotubes, *Chem. – A Eur. J.* 18 (2012) 15283–15287, <https://doi.org/10.1002/chem.201202630>.
- [12] F. Miao, W. Wu, Q. Li, R. Miao, B. Tao, Fabrication and application of molybdenum trioxide nanostructure materials for electrochemical capacitors, *Int. J. Electrochem. Sci.* 12 (2017) 12060–12073, <https://doi.org/10.20964/2017.12.200>.
- [13] E.D. Hanson, L. Lajaunie, S. Hao, B.D. Myers, F. Shi, A.A. Murthy, C. Wolverson, R. Arenal, V.P. David, Systematic study of oxygen vacancy tunable transport properties of few-layer MoO<sub>3</sub> – x enabled by vapor-based synthesis, *Adv. Funct. Mater.* 27 (2017) 1–10, <https://doi.org/10.1002/adfm.201605380>.
- [14] Q. Liu, Y. Wu, J. Zhang, K. Chen, C. Huang, H. Chen, X. Qiu, Plasmonic MoO<sub>3</sub>-x nanosheets with tunable oxygen vacancies as efficient visible light responsive photocatalyst, *Appl. Surf. Sci.* 490 (2019) 395–402, <https://doi.org/10.1016/j.apsusc.2019.06.099>.
- [15] M. Ranjiba, F. Delalat, H. Salamati, Molybdenum oxide nanosheets prepared by an anodizing-exfoliation process and observation of photochromic properties, *Appl. Surf. Sci.* 396 (2017) 1752–1759, <https://doi.org/10.1016/j.apsusc.2016.11.225>.
- [16] J.V. Silveira, J.A. Batista, G.D. Saraiva, J. Mendes Filho, A.G. Souza Filho, S. Hu, X. Wang, Temperature dependent behavior of single walled MoO<sub>3</sub> nanotubes: A Raman spectroscopy study, *Vib. Spectrosc.* 54 (2010) 179–183, <https://doi.org/10.1016/j.vibspec.2010.10.002>.
- [17] T. Kijima, Inorganic and metallic nanotubular materials: recent technologies and applications, *Top. Appl. Phys.* 117 (2010) 83–96, <https://doi.org/10.1007/978-3-642-03622-4>.
- [18] A. Phuruangrat, D.J. Ham, S. Thongtem, J.S. Lee, Electrochemical hydrogen evolution over MoO<sub>3</sub> nanowires produced by microwave-assisted hydrothermal reaction, *Electrochem. Commun.* 11 (2009) 1740–1743, <https://doi.org/10.1016/j.elecom.2009.07.005>.
- [19] J. Zhou, S.Z. Deng, N.S. Xu, J. Chen, J.C. She, Synthesis and field-emission properties of aligned MoO<sub>3</sub> nanowires, *Appl. Phys. Lett.* 83 (2003) 2653–2655, <https://doi.org/10.1063/1.1613992>.
- [20] Y. Li, Y. Bando, Quasi-aligned MoO<sub>3</sub> nanotubes grown on Ta substrate, *Chem. Phys. Lett.* 364 (2002) 484–488, [https://doi.org/10.1016/S0009-2614\(02\)01373-8](https://doi.org/10.1016/S0009-2614(02)01373-8).
- [21] Y. Chen, Z. Fan, Z. Zhang, W. Niu, C. Li, N. Yang, B. Chen, H. Zhang, Two-dimensional metal nanomaterials: synthesis, properties, and applications, *Chem. Rev.* 118 (2018) 6409–6455, <https://doi.org/10.1021/acs.chemrev.7b00727>.
- [22] M. Petr, O. Kylián, A. Kuzminova, J. Kratochvíl, I. Khalakhan, J. Hanuš, H. Biederman, Noble metal nanostructures for double plasmon resonance with tunable properties, *Opt. Mater. (Amst)* 64 (2017) 276–281, <https://doi.org/10.1016/j.optmat.2016.12.021>.
- [23] H. Li, Y. Bian, Selective colorimetric sensing of histidine in aqueous solutions using cysteine modified silver nanoparticles in the presence of Hg<sup>2+</sup>, *Nanotechnology* 20 (2009), <https://doi.org/10.1088/0957-4484/20/14/145502>.
- [24] T. Lou, Z. Chen, Y. Wang, L. Chen, Blue-to-red colorimetric sensing strategy for Hg<sup>2+</sup> and Ag<sup>+</sup> via redox-regulated surface chemistry of gold nanoparticles, *ACS Appl. Mater. Interfaces* 3 (2011) 1568–1573, <https://doi.org/10.1021/am200130e>.
- [25] A. Ravindran, V. Mani, N. Chandrasekaran, A. Mukherjee, Selective colorimetric sensing of cysteine in aqueous solutions using silver nanoparticles in the presence of Cr<sup>3+</sup>, *Talanta* 85 (2011) 533–540, <https://doi.org/10.1016/j.talanta.2011.04.031>.
- [26] Z. Wang, J. Zhang, J. Lv, K. Dai, C. Liang, Plasmonic Ag<sub>2</sub>MoO<sub>4</sub>/AgBr/Ag composite: Excellent photocatalytic performance and possible photocatalytic mechanism, *Appl. Surf. Sci.* 396 (2017) 791–798, <https://doi.org/10.1016/j.apsusc.2016.11.031>.
- [27] G.V. Naik, V.M. Shalav, A. Boltasseva, Alternative plasmonic materials: Beyond gold and silver, *Adv. Mater.* 25 (2013) 3264–3294, <https://doi.org/10.1002/adma.201205076>.
- [28] G.V. Hartland, Optical studies of dynamics in noble metal nanostructures, *Chem. Rev.* 111 (2011) 3858–3887, <https://doi.org/10.1021/cr1002547>.
- [29] K. Yuan, R. Qin, J. Yu, X. Li, L. Li, X. Yang, X. Yu, Z. Lu, X. Zhang, H. Liu, Effects of localized surface plasmon resonance of Ag nanoparticles on luminescence of carbon dots with blue, green and yellow emission, *Appl. Surf. Sci.* 502 (2020) 144277, <https://doi.org/10.1016/j.apsusc.2019.144277>.
- [30] J.S. Duque, J.S. Blandón, H. Riascos, Localized Plasmon resonance in metal nanoparticles using Mie theory, *J. Phys. Conf. Ser.* 850 (2017), <https://doi.org/10.1088/1742-6596/850/1/012017>.
- [31] M. Shabaninezhad, G. Ramakrishna, Theoretical investigation of plasmonic properties of quantum-sized silver nanoparticles, *Plasmonics* (2019), <https://doi.org/10.1007/s10651-019-00000-0>.



- 1007/s11468-019-01102-9.
- [32] B. Doiron, M. Mota, M.P. Wells, R. Bower, A. Mihai, Y. Li, L.F. Cohen, N.M.N. Alford, P.K. Petrov, R.F. Oulton, S.A. Maier, Quantifying figures of merit for localized surface plasmon resonance applications: a materials survey, *ACS Photonics*. 6 (2019) 240–259, <https://doi.org/10.1021/acsp Photonics.8b01369>.
- [33] N. Jiang, X. Zhuo, J. Wang, Active plasmonics: principles, structures, and applications, *Chem. Rev.* 118 (2018) 3054–3099, <https://doi.org/10.1021/acs.chemrev.7b00252>.
- [34] H.M.M.M. Arachchige, E. Comini, D. Zappa, G. Sberveglieri, Gas sensing properties of MoO<sub>3</sub>, *Proceedings*. 1 (2017) 449, <https://doi.org/10.3390/proceedings1040449>.
- [35] A. Borgschulte, O. Sambalova, R. Delmelle, S. Jenatsch, R. Hany, F. Nüesch, Hydrogen reduction of molybdenum oxide at room temperature, *Sci. Rep.* 7 (2017) 1–9, <https://doi.org/10.1038/srep40761>.
- [36] D. Di Yao, J.Z. Ou, K. Latham, S. Zhuyikov, A.P. O'Mullane, K. Kalantar-Zadeh, Electrodeposited  $\alpha$ - and  $\beta$ -phase MoO<sub>3</sub> films and investigation of their gasochromic properties, *Cryst. Growth Des.* 12 (2012) 1865–1870, <https://doi.org/10.1021/cg201500b>.
- [37] M.B. Rahmani, S.H. Keshmiri, J. Yu, A.Z. Sadek, L. Al-Mashat, A. Moafi, K. Latham, Y.X. Li, W. Wlodarski, K. Kalantar-zadeh, Gas sensing properties of thermally evaporated lamellar MoO<sub>3</sub>, *Sensors Actuators, B Chem.* 145 (2010) 13–19, <https://doi.org/10.1016/j.snb.2009.11.007>.
- [38] M. Shafiei, J. Yu, M. Breedon, A. Moafi, K. Kalantar-zadeh, W. Wlodarski, R.B. Kaner, K. Galatsis, Pt/MoO<sub>3</sub> nano-flower/SiC schottky diode based hydrogen gas sensor, *Proc. IEEE Sensors* (2010) 354–357, <https://doi.org/10.1109/ICSENS.2010.5690245>.
- [39] M. Ferroni, V. Guidi, G. Martinelli, P. Nelli, M. Sacerdoti, G. Sberveglieri, Characterization of a molybdenum oxide sputtered thin film as a gas sensor, *Thin Solid Films* 307 (1997) 148–151, [https://doi.org/10.1016/S0040-6090\(97\)00279-4](https://doi.org/10.1016/S0040-6090(97)00279-4).
- [40] M.E. Stewart, C.R. Anderton, L.B. Thompson, J. Maria, S.K. Gray, J.A. Rogers, R.G. Nuzzo, Nanostructured plasmonic sensors, *Chem. Rev.* 108 (2008) 494–521, <https://doi.org/10.1021/cr068126n>.
- [41] A. Agrawal, S.H. Cho, O. Zandi, S. Ghosh, R.W. Johns, D.J. Milliron, Localized surface plasmon resonance in semiconductor nanocrystals, *Chem. Rev.* 118 (2018) 3121–3207, <https://doi.org/10.1021/acs.chemrev.7b00613>.
- [42] M.B. Ross, C.A. Mirkin, G.C. Schatz, Optical properties of one-, two-, and three-dimensional arrays of plasmonic nanostructures, *J. Phys. Chem. C* 120 (2016) 816–830, <https://doi.org/10.1021/acs.jpcc.5b10800>.
- [43] H. Yin, Y. Kuwahara, K. Mori, H. Cheng, M. Wen, Y. Huo, H. Yamashita, Localized surface plasmon resonances in plasmonic molybdenum tungsten oxide hybrid for visible-light-enhanced catalytic reaction, *J. Phys. Chem. C* 121 (2017) 23531–23540, <https://doi.org/10.1021/acs.jpcc.7b08403>.
- [44] Gaspera, Rigon, Martucci, Optical gas sensors based on localised surface plasmon resonance, *Proceedings* 14 (2019) 19, <https://doi.org/10.3390/proceedings2019014019>.
- [45] M. Wang, P. Wang, J. Zhang, H. Hou, C. Li, Y. Jin, Pd/Ag nanosheet as a plasmonic sensing platform for sensitive assessment of hydrogen evolution reaction in colloid solutions, *Nano Res.* 11 (2018) 2093–2103, <https://doi.org/10.1007/s12274-017-1827-5>.
- [46] M.S. Barbosa, P.H. Suman, J.J. Kim, H.L. Tuller, J.A. Varela, M.O. Orlandi, Gas sensor properties of Ag- and Pd-decorated SnO micro-disks to NO<sub>2</sub>, H<sub>2</sub> and CO: Catalyst enhanced sensor response and selectivity, *Sensors Actuators, B Chem.* 239 (2017) 253–261, <https://doi.org/10.1016/j.snb.2016.07.157>.
- [47] M.A. Hosseini, M. Ranjbar, M. Sajadi, Au-MoO<sub>x</sub> nanoparticles for LSPR hydrogen detection prepared by a facile anodizing method, *Phys. Lett. Sect. A Gen. At. Solid State Phys.* 384 (2020) 126079, <https://doi.org/10.1016/j.physleta.2019.126079>.
- [48] M.A. Hosseini, M. Ranjbar, Plasmonic Au-MoO<sub>3</sub> colloidal nanoparticles by reduction of H<sub>2</sub>AuCl<sub>4</sub> by blue MoO<sub>x</sub> nanosheets and observation of the gasochromic property, *Plasmonics* 13 (2018) 1897–1906, <https://doi.org/10.1007/s11468-018-0704-8>.
- [49] J.Z. Ou, J.L. Campbell, D. Yao, W. Wlodarski, K. Kalantar-Zadeh, In situ Raman spectroscopy of H<sub>2</sub> gas interaction with layered MoO<sub>3</sub>, *J. Phys. Chem. C* 115 (2011) 10757–10763, <https://doi.org/10.1021/jp202123a>.
- [50] R.S. Datta, F. Haque, M. Mohiuddin, B.J. Carey, N. Syed, A. Zavabeti, B. Zhang, H. Khan, K.J. Berean, J.Z. Ou, N. Mahmood, T. Daeneke, K. Kalantar-Zadeh, Highly active two dimensional  $\alpha$ -MoO<sub>3</sub>: X for the electrocatalytic hydrogen evolution reaction, *J. Mater. Chem. A* 5 (2017) 24223–24231, <https://doi.org/10.1039/c7ta07705j>.
- [51] W. Liu, Q. Xu, W. Cui, C. Zhu, Y. Qi, CO<sub>2</sub>-assisted fabrication of two-dimensional amorphous molybdenum oxide nanosheets for enhanced plasmon resonances, *Angew. Chem. – Int. Ed.* 56 (2017) 1600–1604, <https://doi.org/10.1002/anie.201610708>.
- [52] U.R. Kortshagen, R.M. Sankaran, R.N. Pereira, S.L. Girshick, J.J. Wu, E.S. Aydil, Nonthermal plasma synthesis of nanocrystals: Fundamental principles, materials, and applications, *Chem. Rev.* 116 (2016) 11061–11127, <https://doi.org/10.1021/acs.chemrev.6b00039>.
- [53] J.I. Gu, J. Lee, C.K. Rhee, Y. Sohn, Enhanced electrochemical hydrogen evolution over defect-induced hybrid MoO<sub>3</sub>/Mo<sub>3</sub>O<sub>9</sub>H<sub>2</sub>O microrods, *Appl. Surf. Sci.* 469 (2019) 348–356, <https://doi.org/10.1016/j.apsusc.2018.11.050>.
- [54] A.H. Odda, Y. Xu, J. Lin, G. Wang, N. Ullah, A. Zeb, K. Liang, L.P. Wen, A.W. Xu, Plasmonic MoO<sub>3</sub>-x nanoparticles incorporated in Prussian blue frameworks exhibit highly efficient dual photothermal/photodynamic therapy, *J. Mater. Chem. B* 7 (2019) 2032–2042, <https://doi.org/10.1039/c8tb03148g>.
- [55] M.A. Hosseini, M. Ranjbar, A.R. Shafieyan, Flame synthesis of MoO<sub>3</sub> films and their flame reduction to MoO<sub>3</sub>-X Films for NIR-shielding applications, *Surf. Rev. Lett.* 27 (2020) 1950110, <https://doi.org/10.1142/S0218625X19501105>.
- [56] M.M.Y.A. Alsaif, M.R. Field, T. Daeneke, A.F. Chrimes, W. Zhang, B.J. Carey, K.J. Berean, S. Walia, J. Van Embden, B. Zhang, K. Latham, K. Kalantar-Zadeh, J.Z. Ou, Exfoliation solvent dependent plasmon resonances in two-dimensional sub-stoichiometric molybdenum oxide nanoflakes, *ACS Appl. Mater. Interfaces* 8 (2016) 3482–3493, <https://doi.org/10.1021/acsami.5b12076>.
- [57] A. Borgschulte, O. Sambalova, R. Delmelle, S. Jenatsch, R. Hany, F. Nüesch, Hydrogen reduction of molybdenum oxide at room temperature, *Sci. Rep.* 7 (2017) 40761, <https://doi.org/10.1038/srep40761>.
- [58] W.V. Schulmeyer, H.M. Ortnier, Mechanisms of the hydrogen reduction of molybdenum oxides, *Int. J. Refract. Met. Hard Mater.* 20 (2002) 261–269, [https://doi.org/10.1016/S0263-4368\(02\)00029-X](https://doi.org/10.1016/S0263-4368(02)00029-X).
- [59] B.S. Kim, E.Y. Kim, H.S. Jeon, H.I. Lee, J.C. Lee, Study on the reduction of molybdenum dioxide, by hydrogen, *Mater. Trans.* (2008), <https://doi.org/10.2320/matertrans.MER2008103>.
- [60] X. Sha, L. Chen, A.C. Cooper, G.P. Pez, H. Cheng, Hydrogen absorption and diffusion in bulk  $\alpha$ -MoO<sub>3</sub>, *J. Phys. Chem. C* (2009), <https://doi.org/10.1021/jp9017212>.
- [61] J. Dang, G.-H. Zhang, K.-C. Chou, R.G. Reddy, Y. He, Y. Sun, Kinetics and mechanism of hydrogen reduction of MoO<sub>3</sub> to MoO<sub>2</sub>, *Int. J. Refract. Met. Hard Mater.* 41 (2013) 216–223, <https://doi.org/10.1016/j.jrmhm.2013.04.002>.
- [62] T. Matsuda, Y. Hirata, H. Itoh, H. Sakagami, N. Takahashi, Effect of reduction temperature on the transformation of MoO<sub>3</sub> to MoO<sub>x</sub> with a large surface area, *Microporous Mesoporous Mater.* (2001), [https://doi.org/10.1016/S1387-1811\(00\)00342-5](https://doi.org/10.1016/S1387-1811(00)00342-5).
- [63] J. Dang, G.-H. Zhang, K.-C. Chou, Phase transitions and morphology evolutions during hydrogen reduction of MoO<sub>3</sub> to MoO<sub>2</sub>, *High Temp. Mater. Process.* 33 (2014) 305–312, <https://doi.org/10.1515/htmp-2013-0061>.
- [64] T. Ressler, J. Wienold, R.E. Jentoft, Formation of bronzes during temperature-programmed reduction of MoO<sub>3</sub> with hydrogen – An in situ XRD and XAFS study, *Solid State Ionics* (2001), [https://doi.org/10.1016/S0167-2738\(01\)00747-0](https://doi.org/10.1016/S0167-2738(01)00747-0).
- [65] Jim Clark, *absorption spectra – the Beer-Lambert Law*, Chemguide (2017).
- [66] W. Xie, M. Su, Z. Zheng, Y. Wang, L. Gong, F. Xie, W. Zhang, Z. Luo, J. Luo, P. Liu, N. Xu, S. Deng, H. Chen, J. Chen, Nanoscale insights into the hydrogenation process of layered  $\alpha$ -MoO<sub>3</sub>, *ACS Nano*. 10 (2016) 1662–1670, <https://doi.org/10.1021/acsnano.5b07420>.
- [67] H. Cheng, M. Wen, X. Ma, Y. Kuwahara, K. Mori, Y. Dai, B. Huang, H. Yamashita, Hydrogen doped metal oxide semiconductors with exceptional and tunable localized surface plasmon resonances, *J. Am. Chem. Soc.* 138 (2016) 9316–9324, <https://doi.org/10.1021/jacs.6b05396>.